ACS APPLIED MATERIALS & INTERFACES

www.acsami.org Research Article

Direct-Write of Nanoscale Domains with Tunable Metamagnetic Order in FeRh Thin Films

Cory D. Cress,* Darshana Wickramaratne, Matthew R. Rosenberger, Zachariah Hennighausen, Patrick G. Callahan, Samuel W. LaGasse, Noam Bernstein, Olaf M. van 't Erve, Berend T. Jonker, Syed B. Qadri, Joseph C. Prestigiacomo, Marc Currie, Igor I. Mazin, and Steven P. Bennett*

Cite This: *ACS Appl. Mater. Interfaces* 2021, 13, 836–847 Read Online

ACCESS | Metrics & More | Article Recommendations | Supporting Information

ABSTRACT: We have directly written nanoscale patterns of magnetic ordering in FeRh films using focused helium-ion beam irradiation. By varying the dose, we pattern arrays with metamagnetic transition temperatures that range from the as-grown film temperature to below room temperature. We employ transmission electron microscopy, X-ray diffraction, and temperature-dependent transport measurements to characterize the as-grown film, and magneto-optic Kerr effect imaging to quantify the He^+ irradiation-induced changes to the magnetic order. Moreover, we demonstrate temperature-dependent optical microscopy and conductive atomic force microscopy as indirect probes of the metamagnetic transition that are sensitive to the differences in dielectric properties and electrical conductivity, respectively, of FeRh in the antiferromagnetic (AF) and ferromagnetic (FM) states. Using density functional theory, we quantify strain- and defect-induced changes in spin-flip energy to understand their influence on the metamagnetic transition temperature. This work holds promise for in-plane AF−FM spintronic devices, by reducing the need for multiple patterning steps or different materials, and potentially eliminating interfacial polarization losses due to cross material interfacial spin scattering.

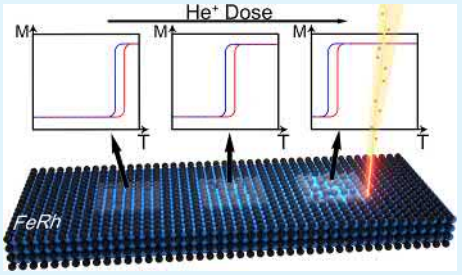

KEYWORDS: *helium ion microscopy, FeRh, metamagnetic, antiferromagnetic, tunable magnetic transition*

INTRODUCTION

The recent advent of antiferromagnetic (AF) spintronics has ushered in a new toolbox of ultrahigh speed spin physics to the nanoscale electronics community.[1−4] The community is currently racing to understand the fundamental physics of a sought-after AF memory by building test device configurations to probe new types of AF materials and device geometries. The vast majority of these studies rely on the creation of multiple magnetic orderings in intimate contact using both lateral[5,6] and vertical[3,4] heterostructures of multiple materials. The ability to monolithically couple regions of AF and ferromagnetic (FM) order, similar to that achieved in thin films of $FePt_3$ at low temperature (below $T_{Néel}$ = 160 K),[7] could eliminate the complications associated with interfaces and concomitant interfacial polarization losses, thus yielding a uniquely capable material system for applications in the AF spintronics domain. FeRh is a room-temperature antiferromagnet, which exhibits a process-tunable AF to FM (i.e., metamagnetic) transition above 360 K,[8] thereby making it a top candidate material for this role.[9−12]

FeRh is a binary metallic compound with a unique metamagnetic transition from AF to FM ordering at ∼360 K in the bulk, resulting in an unparalleled change in magnetization (∼800 emu/cm^3) and a ∼1.0% lattice expansion.[13] The relatively high temperature of this transition distinguishes FeRh from all other metamagnetic materials whose transitions are at or below room temperature [e.g., $FeCl_2$ (∼20 K),[14] $La(Fe, Si)_{13}$ (∼200 K),[15] UPt_3 (∼1.5 K),[16] and $YMn_6Sn_{6-x}Ti_x$ (∼293 K)[17]]. Much of the current understanding of the FeRh metamagnetic transition derives from studies of the bulk material performed nearly 60 years ago.[13,18,19] A resurgence of interest is driven by its potential use in a plethora of thin-film-based applications including magnetic memory,[20,21] AF electronics,[20,22,23] and magnetocalorics.[24] Recent work on FeRh has demonstrated a very high sensitivity to strain[25−29] as well as ultrahigh speed critical point dynamics.[30] Additionally, the origin of the microscopic driving force for the transition has been the focus of numerous theoretical studies,[31−34] which have not led to a consensus.

Integration of FeRh into new AF spintronic applications relies on both controlling (i.e., tuning the temperature) and establishing a trigger (a switch) for the metamagnetic transition. To tune the transition temperature, a number of studies have demonstrated the effects of dilute alloys wherein

Received: July 28, 2020
Accepted: November 9, 2020
Published: November 20, 2020

https://dx.doi.org/10.1021/acsami.0c13565
ACS Appl. Mater. Interfaces 2021, 13, 836−847

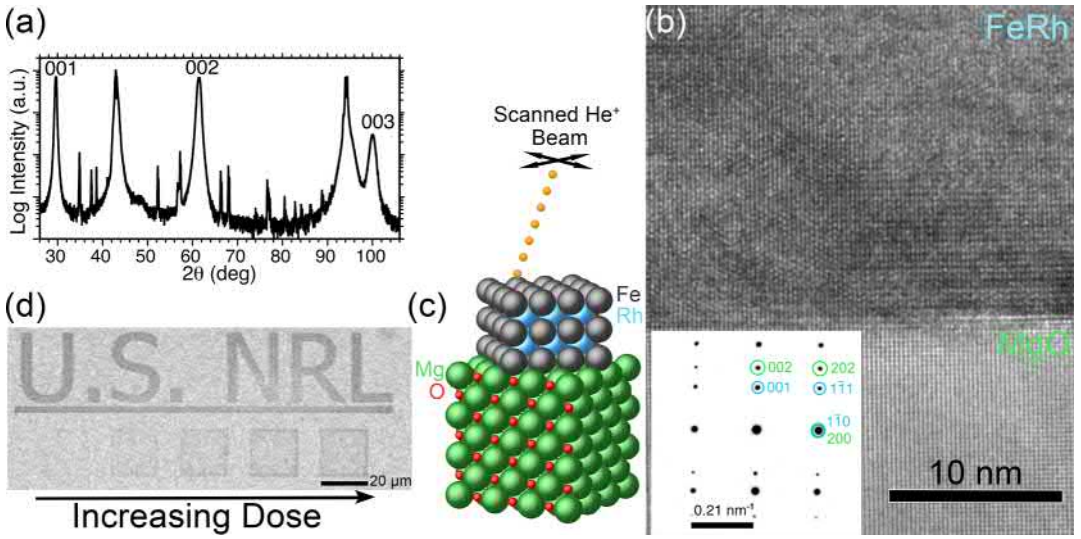

Figure 1. (a) XRD $\theta-2\theta$ scan with FeRh reflections indexed. (b) HR-TEM image of the FeRh−MgO interface and the corresponding SADP pattern. (c) Schematic depiction of the sample layers and processing of the films; a He^+ beam is scanned over the surface of the FeRh. (d) Helium ion micrograph of an FeRh film surface immediately after implantation revealing greater contrast in the highest dose regions (dose: 1.1×10^{14}, 2.2×10^{14}, 4.0×10^{14}, 6.2×10^{14}, and 8.0×10^{14} He^+ cm^{-2}; U.S. NRL lettering dose 1×10^{15} He^+ cm^{-2}). Scale bar: 20 μm.

transition metals, such as Pt, Pd, Ir, Cu, Au, and so forth, incorporated at ∼0.1−5% concentration, either decrease or increase the transition temperature.[35−37] However, more recently it has been shown that the direct incorporation of defects that do not change the composition, by either light or heavy ion irradiation, can be highly effective at reducing the transition temperature.[8,38−45]

In this work, we demonstrate the use of a helium ion microscope to directly write nanoscale regions of controlled magnetic ordering in a film of FeRh, which exhibits either AF order or FM order, and tune the AF−FM metamagnetic transition temperature over a 125 K range. As a focused ion beam (FIB) technique, but with a nearly atomic scale probe size, helium ion microscopy (HIM) continues to find a broadening application space beyond microscopy, to include high-precision ion milling,[46] irradiation studies with submicron features,[47] and precise defect engineering.[48,49] Using the HIM, and through a combination of optical microscopy, magneto-optic Kerr effect (MOKE) imaging, and conductive atomic force microscopy (CAFM), we show that nanoscale regions can be reproducibly written in confined geometries down to 25 nm. Using first-principles calculations based on density functional theory, we study the impact of probable He^+-induced point defects and quantify their influence on the spin-flip energy, a parameter related to the metamagnetic transition temperature.

Physical Characterization. Figure 1a shows the $\theta-2\theta$ X-ray diffraction (XRD) pattern of a 200 nm thick FeRh film grown by sputter deposition on MgO(001) (see Methods). Each of the primary FeRh reflections is labeled, and the other intense reflections belong to the MgO substrate. The third order peak position (003) of $2\theta = 100.036°$ corresponds to a c-axis lattice spacing of ∼3.02 Å, while the full width at half-maximum of 0.4° for the (001) reflection is indicative of fully-dense phase-pure epitaxial near-stochiometric FeRh films.[11] Temperature-dependent XRD measurements reveal the characteristic expansion in the lattice parameter, and the crystallite size with temperature, consistent with a first-order transition (see Figure S1). Additionally, we prepared electron transparent slices through the FeRh/MgO (001) interface using standard FIB lift-out techniques (see Methods) for high-resolution transmission electron microscopy (HR-TEM) analysis. The HR-TEM lattice image and selected area electron diffraction pattern (SADP) shown in Figure 1b confirm the fully dense nature and epitaxial alignment of the FeRh to the MgO substrate. The three-dimensional representative schematic in Figure 1c shows the 45° rotated growth of FeRh and MgO [100] crystal axes, which is confirmed by the SADP of Figure 1b where we observe overlapping in-plane $(1\bar{1}0)$-FeRh and (200)-MgO reflections.[8,22,26]

We employ the highly focused 30 keV He^+ beam (diameter <1 nm) of a helium ion microscope to achieve spatially controlled regions of FeRh with dose-dependent metamagnetic transition temperatures (1×10^{14} <He^+ dose <5×10^{16} cm^{-2}). Following the automated pattern writing process, we captured a short-integration/low-resolution (i.e., He^+ dose <1×10^{11} He^+ cm^{-2}) helium ion micrograph of the processed region (Figure 1d), which shows a dose-dependent contrast. The origin of the contrast is hypothesized to stem from a decrease in conductivity throughout the volume of the dosed regions, which is consistent with CAFM measurements presented below for doses below 3.6×10^{15} He^+/cm^2. Other possible sources of increased contrast may be related to changes in the secondary electron emissivity resulting from an increased surface work function, adsorption/desorption of surface contaminants, and changes in the dielectric properties. A thin (<10 nm) layer of deposited carbon, primarily at the edges of the highest dosed features and common to such FIB processes, may also contribute to the image contrast (see Figure S2).[50] The nanoscale features, discussed later, are processed with a single raster scan of the beam, which largely mitigates unwanted carbon deposition and yields reductions in the film height at the highest doses.

Tuning the Metamagnetic Transition Temperature. We employ both MOKE microscopy and optical microscopy to investigate the He^+ dose-dependent changes in our FeRh films. Figure 2a displays the room-temperature Kerr rotation as a function of in-plane magnetic field (longitudinal MOKE

https://dx.doi.org/10.1021/acsami.0c13565
ACS Appl. Mater. Interfaces 2021, 13, 836−847

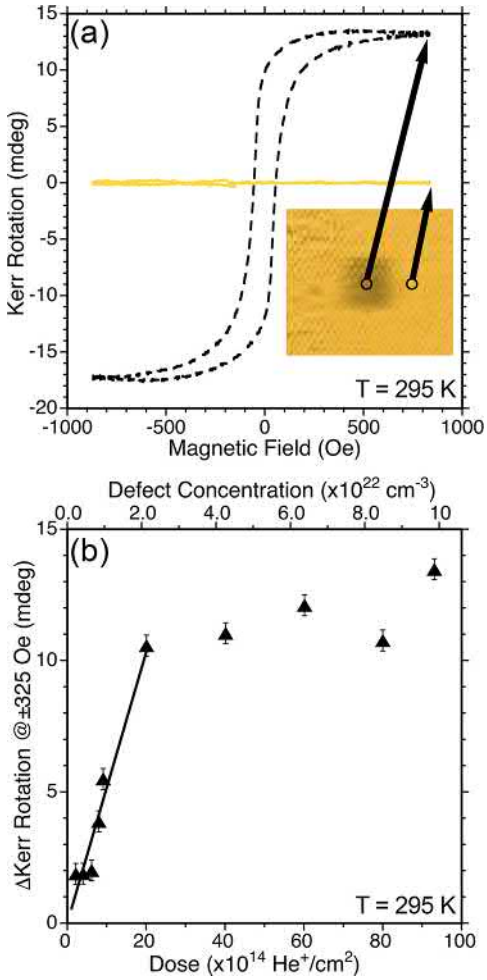

Figure 2. (a) Kerr rotation vs magnetic field for a pristine FeRh film (yellow) and within a square region dosed with 8.5×10^{15} He^+ cm^{-2} (gray line). Inset: Corresponding MOKE image illustrating the magnetic contrast in the dosed region; scale bar: 100 μm. (b) Kerr rotation as a function of He^+ dose.

geometry) for a region of the as-grown FeRh film and an adjacent region implanted with $\sim 8.5 \times 10^{15}$ He^+ cm^{-2}. The inset of Figure 2a contains a MOKE image taken at ~850 Oe, which depicts a region of high contrast (i.e., high Kerr rotation) coinciding with the He^+-implanted region. The effect of implantation is clearly evident when comparing it with the room-temperature magnetic-field-dependent Kerr rotation measurement of the pristine film. In the AF state, the pristine FeRh displays no Kerr response. Conversely, the He^+ implantation causes the magnetostructural transition of FeRh to shift below room temperature, producing the FM state and leading to Kerr rotation that mimics a typical magnetization hysteresis loop consistent with a FM domain.

The ability to direct-write multiple features into a single FeRh film enables us to measure the room-temperature Kerr rotation simultaneously for a series of different doses. In Figure 2b, we investigate the room-temperature Kerr rotation for He^+ doses ranging from $\sim 1 \times 10^{14}$ to 1×10^{16} He^+ cm^{-2}. Here, we observe a dose-dependent linear increase in Kerr rotation with the sample reaching a saturated Kerr rotation of 12.5 mdeg at a dose of $\sim 2 \times 10^{15}$ He^+ cm^{-2}, and persisting beyond 1×10^{16} He^+ cm^{-2}. In the linear regime, the slope is 5.2 mdeg per 10^{15} He^+ cm^{-2}. Transport of ions in matter (TRIM) simulations determine a penetration depth peak of 110 nm with a longitudinal straggle of 46 nm, meaning a majority of the He^+ come to rest within the base of the film near the MgO substrate.[51] The peak defect concentration also occurs in this location (see Figure S3). In contrast, the peak ionizing energy loss occurs within the top 50 nm of the film and decreases approximately linearly with depth. Using a computed value of 212 defects per ion based on TRIM simulations, the saturating dose of 2×10^{15} He^+ cm^{-2} yields a mean defect density of 2.1×10^{22} cm^{-3}. Interestingly, the onset of FM saturation is similar to the saturated magnetization reported for a defect concentration of $\sim 1.5 \times 10^{22}$ cm^{-3} induced by 20 keV Ne^+ irradiations [measured by superconducting quantum interference device (SQUID)/vibrating sample magnetometer] in 35 nm FeRh films.[44] This close correlation is achieved despite the fact that 20 keV Ne^+ ions have a nuclear stopping power ~30× greater than 30 keV He^+.[51,52] Greater defect generation rates typically yield larger defect clusters; therefore, the fact that saturation occurs at approximately the same total defect concentration (all Frenkel pairs treated as one defect) suggests that point defects are sufficient to modify the metamagnetic transition rather than a particular defect complex.

The results reported above are consistent with prior broad-area irradiation studies with low-energy He,[8] Ne,[42,44,53,54] and Ga ions.[44] Furthermore, in a previous study, the magnetic moment induced per unit fluence of swift heavy ions including Ni, Kr, Xe, and Au[55] was reported to correlate positively for both the nuclear stopping power and the electronic stopping power of each of the respective ions. However, the limited range of stopping powers studied precluded the determination of the primary ion-matter interaction responsible for the change. The nuclear stopping power of 30 keV He^+ (12.5 MeV cm^2 g^{-1}) is 3× to 40× less than the nuclear stopping powers of the swift heavy ions, yet has an electronic stopping power (166.3 MeV cm^2 g^{-1}) that is 120× to 275× less than that of the swift heavy ions, and thus provides the additional range of stopping powers needed to make a determination. Based on our observed saturating dose of 2×10^{15} He^+ cm^{-2}, which is between 3× and 40× more fluence than the swift heavy ions, we conclude that nuclear stopping, that is, ion-matter energy transfers to the lattice, that are primarily in the form of vacancies, are the prevailing source of changes in the magnetic moment in ion-irradiated FeRh. If the electronic interactions were the dominant ion-matter energy transfer mechanism, a dose in excess of 1.2×10^{16} He^+ cm^{-2} would be the minimum predicted dose needed to saturate the response.

In Figure 3a, we plot the temperature-dependent conductivity of an as-grown FeRh film grown on MgO based on 4-probe measurements. Below the transition temperature, we observe a monotonic decrease in conductivity with increasing temperature (upward triangles), typical of metals. At ~405 K, the conductivity abruptly increases before once again displaying metallic behavior above 460 K. During cooling (downward triangles), we observe the reverse behavior but with a hysteresis of approximately 15 K. Beginning with a room-temperature conductivity of 3 kS cm^{-1}, the conductivity decreases to a minimum of 2.2 kS cm^{-1} and then goes up to a maximum of 3.5 kS cm^{-1}, that is, the conductivity ranges from −27 to +17% compared to the room-temperature conductivity. We also plot the temperature-dependent magnetic moment (magenta line) in Figure 3a measured via SQUID (see Methods). On the heating cycle, the onset of the metamagnetic transition begins at ~405 K, consistent with the conductivity,

https://dx.doi.org/10.1021/acsami.0c13565
ACS Appl. Mater. Interfaces 2021, 13, 836−847

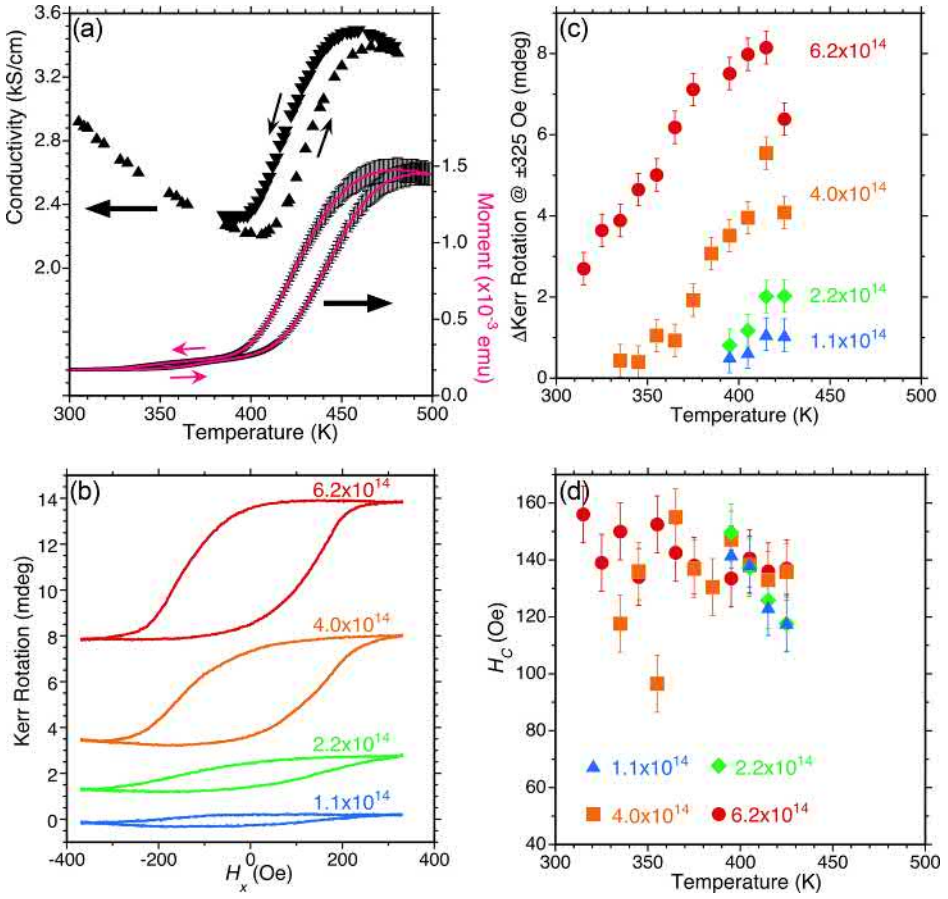

Figure 3. (a) Left *y*-axis corresponds to four-probe temperature-dependent conductivity for the FeRh film for increasing (upward triangles) and decreasing temperature (downward triangles) along with the temperature-dependent magnetic moment on the right *y*-axis measured at 100 Oe. (b) Magnetic field-dependent Kerr rotation at 415 K for films irradiated with doses ranging from 1.1×10^{14} to 6.2×10^{14} He^+ cm^{-2}, with each trace vertically offset for clarity. (c,d) The temperature-dependent (c) change in Kerr rotation at ±325 Oe and (d) coercivity measured in films with He^+ implantation doses ranging from 1.1×10^{14} to 6.2×10^{14} He^+ cm^{-2}, as labeled.

and it also displays a hysteresis of ∼15 K. This demonstrates the correlation between the temperature-dependent conductivity and the magnetism of the FeRh, both of which are strongly influenced by the metamagnetic transition.

Because of the limited spatial resolution of SQUID magnetometry, we employ the use of MOKE imaging to investigate the metamagnetic transition in micron-scale He^+-patterned FeRh films. In Figure 3b, we show the Kerr rotation as a function of magnetic field at 415 K for four regions patterned with increasing He^+ doses. As the He^+ dose increases, the transition moves to lower temperatures leading to larger increases in Kerr rotation and widening of the hysteresis width. From a systematic series of MOKE measurements, we extract both the change in Kerr rotation at ±325 Oe (i.e., ΔKerr rotation = Kerr rotation @ +325 Oe − Kerr rotation @ −325 Oe) and the coercivity (H_c) for temperatures ranging from ∼300 to 425 K for four different He^+ doses measured simultaneously (for a given temperature) ranging from 1.1×10^{14} to 6.2×10^{14} He^+ cm^{-2}. At the two lowest doses, a measurable ΔKerr rotation is observed at 390 K Figure 3c, a point that is about 15 K below the onset of the as-grown film transition temperature based on the conductivity and SQUID data. Above 390 K, the Kerr rotation increases gradually for both regions, with a slightly larger magnitude for the region implanted with a higher dose of 2.2×10^{14} He^+ cm^{-2}. The FeRh regions implanted with doses of 4.0×10^{14} and 6.2×10^{14} He^+ cm^{-2} show a large temperature dependence in the ΔKerr rotation increasing until reaching 415 K. In these regions, the apparent onset of the metamagnetic transition decreases by approximately 55 and 100 K from that of the 1.1×10^{14} He^+ cm^{-2} dose, respectively. This amounts to a decrease of ∼1 K per 5×10^{12} He^+ cm^{-2}, or using the He^+ defect formation rate of 212 def per He^+, a decrease of ∼1 K per 5.3×10^{19} def cm^{-3}. To put this in perspective, the latter value corresponds to a volume per defect $V_D = 18.9$ nm^3 def^{-1} for a mean interdefect distance of $L_D = \sqrt[3]{V_D} \cong 2.7$ nm. At a saturating dose of 2×10^{15} cm^{-2}, the mean interdefect distance decreases to 0.36 nm or about 1 defect per 3.5 atoms. This is a logical saturating condition because, on average, every atom is adjacent to at least one defect that breaks the local symmetry and thus additional defects have little effect. With increasing dose, we expect a reduction in ΔKerr rotation saturation temperature, the onset of which may be occurring in the sample irradiated with a dose of 6×10^{14} He^+ cm^{-2} above 395 K. Additionally, the more gradual increase in ΔKerr rotation and H_c, as compared to the lower dose results may indicate a broadening of the transition. Even at this level of damage, however, we are able to recover the AF spin alignment in the film by annealing in 5 mTorr Ar for 1 h at 730 °C (i.e., the standard postgrowth annealing process).[8]

In contrast to the ΔKerr rotation, the coercivity H_c in these regions shows an inverse temperature dependence, especially

https://dx.doi.org/10.1021/acsami.0c13565
ACS Appl. Mater. Interfaces 2021, 13, 836−847

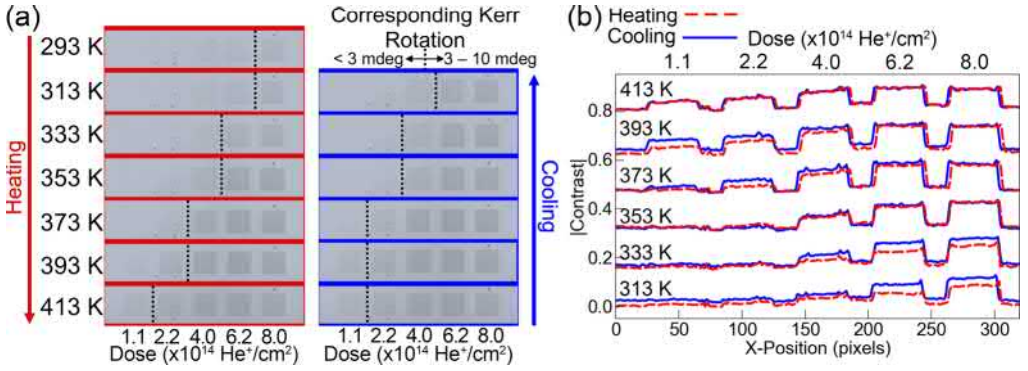

Figure 4. (a) Temperature-dependent optical microscopy images for the heating and cooling cycle of an FeRh film processed with five different He^+ doses as labeled. Squares = 20 μm. (b) Optical contrast vs x-position extracted from the images in part (a) measured during sample heating (red dashed lines) and cooling (blue lines).

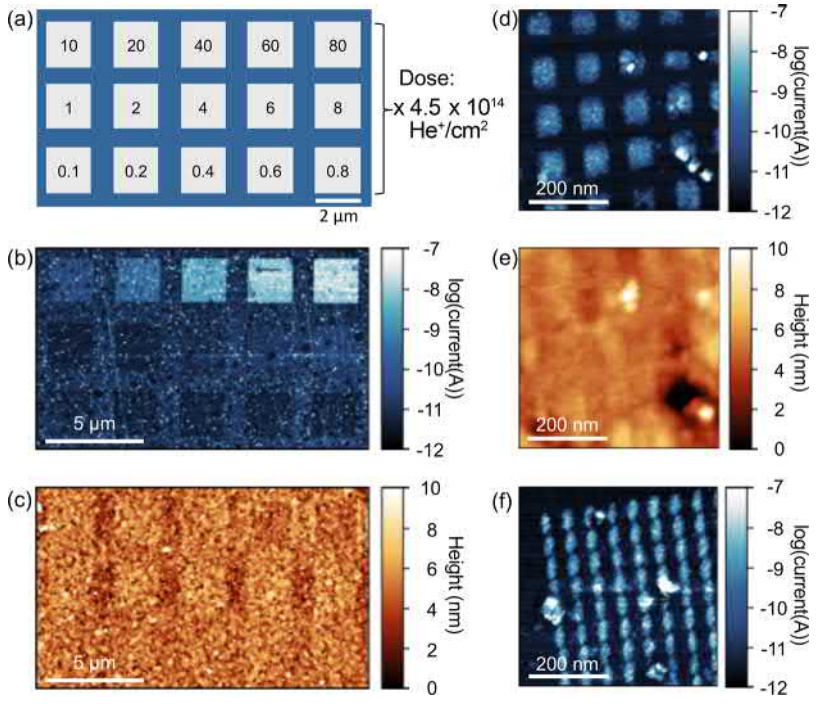

Figure 5. CAFM of an FeRh film after He ion exposure. (a) Diagram of the dose test grid for sample measured in (b,c). (b) CAFM current measurement on the log scale showing a strong dependence of current on dose. (c) CAFM height measurement showing small changes in height due to He^+ exposure. (d) CAFM current measurement on the log scale of 50 nm square pixels written with a pitch of 100 nm. (e) CAFM height measurements corresponding to (d). (f) CAFM current measurement on the log scale of spot array exposure with a dose of 2.0×10^5 He^+/spot.

for the two lowest doses. In these areas, H_c decreases from 140 to 118 Oe for the lowest dose and from 150 to 118 Oe for the 2.2×10^{14} He^+ cm^{-2} dose, as shown in Figure 3d. For the 4.0×10^{14} He^+ cm^{-2} dose, H_c appears to fluctuate significantly below about 360 K when the ΔKerr rotation signal is small, then saturates at elevated temperatures. We observe a similar saturated trend with less fluctuation for the highest dosed region. The decreasing H_c with temperature observed for the lower doses behaves similar to that reported by Arregi et al., for spatially confined FeRh mesoscale rectangles and is attributed to the presence of intermixed AF and FM domains.[56] The modified behavior in H_c at the higher doses may stem from differences in AF and FM domain distribution and formation of pinning centers within the FeRh film because of the use of He^+ irradiation, rather than spatial confinement and shape anisotropy, warranting further studies on these effects.

MOKE imaging has been used to observe the changes in FeRh with dose (as shown in Figure 2a), as well as other features such as spatial confinement effects in <500 nm features.[56] Indeed, we use this technique to observe dose- and temperature-dependent features in FeRh films where features appear with increasing temperature (Figure 3a) or diminish with decreasing temperature (i.e., regions with threshold temperature <295 K) as shown in Figure S4. The direct relation between the MOKE contrast and the degree of magnetization in the film makes it an extremely powerful technique.

Here, we also demonstrate the use of optical microscopy to observe the metamagnetic transition by exploiting the fact that the dielectric function, and therefore the optical reflectance, of FeRh varies spectrally between the AF and FM states,[57] enabling easy identification of its magnetic state with an optical microscope. In Figure 4a, we display optical microscopy

https://dx.doi.org/10.1021/acsami.0c13565
ACS Appl. Mater. Interfaces 2021, 13, 836−847

images of the surface of a processed FeRh film during the heating (left) and cooling (right) cycles. The corresponding image contrast, obtained by averaging the same sampling area within each image, for the heating series (red) and cooling series (blue), is shown in Figure 4b. At 293 K, the 8.0×10^{14} He^+ cm^{-2} dose is immediately apparent as a region of higher contrast than the film or any of the other processed squares. As the temperature increases, the contrast of this region increases further and upon reaching 333 K, the region processed at 6.2×10^{14} He^+ cm^{-2} becomes much more apparent. This trend continues with additional heating, with the dashed line indicating approximately the point when the Kerr rotation exceeds 3 mdeg. During cooling, we observe the opposite behavior with feature contrast diminishing as the temperature decreases, but also with a ~20 K hysteresis in temperature in comparison to the appearance of the feature during heating. This hysteresis is most evident in Figure 4b where the blue and red traces do not overlap for the heating and cooling cycles. Most notably, for the lowest two doses a significant hysteresis is observed at 393 and 373 K (near the as-grown FeRh transition), while for the highest two doses the hysteresis is greatest at the reduced temperatures of 333 and 313 K (also see Figure S5).

Patterning Nanoscale Features. To explore the limits on the minimum feature size we are able to pattern with the HIM, we generate a series of micron and submicron features patterned with a range of doses consisting of a dose series, arrays of nanoscale squares, and a fixed-location spot array. To characterize these samples, we used CAFM to measure local changes in conductance. CAFM consists of AFM in contact mode with an electrical bias applied between the conducting AFM tip and sample. As the surface topography of the sample is measured based on tip deflection, the tip current is measured simultaneously, generating a spatial current map that is proportional to the tip−sample conductance. We infer that the conductivity of the FeRh film at a given temperature will change as a function of He^+ dose based on Figure 3a and the fact that the AF−FM transition temperature (i.e. the dip in Figure 3a) decreases with He^+ dose. Additionally, He^+ irradiation may modify the FeRh surface conductance caused by desorption (e.g., oxygen) or deposition (e.g., carbon) of surface impurities, or via sputtering the surface of the FeRh film. Stemming from either of these mechanisms, we are able to use the CAFM signal as a means to resolve the He^+ dosed regions and the spatial extent of the He^+ modification.

The CAFM results are shown in Figure 5, beginning with the dose pattern in Figure 5a, the CAFM current map in Figure 5b, and the corresponding AFM height map in Figure 5c. The magnitude of the CAFM current shows a clear dose dependence. Compared to the background current (i.e., outside of the patterned squares), the measured current decreases slightly with increasing He^+ dose up to $\sim 4.5 \times 10^{14}$ He^+ cm^{-2}. This decrease in current is consistent with the bulk conductivity measurement in Figure 3a, which indicates that the FeRh conductivity decreases before the material transitions from the AF state to the FM state. The decrease in conductivity in the current context could stem from static defect scattering rather than dynamic temperature-induced phonon scattering.[53] Above 9×10^{14} He^+ cm^{-2}, the measured current increases monotonically with increased He^+ dose. This increase in current is consistent with the increase in current observed in Figure 3a as the material transitions from AF to FM. In general, the qualitative behavior of CAFM current as a function of He^+ dose is consistent with Figure 3a and the fact that the AF−FM transition temperature decreases for increasing He^+. However, the >100× increase in current for doses increasing from 3.6×10^{15} to 3.6×10^{16} He^+ cm^{-2} exceeds the small changes in conductivity observed in Figure 3a. This observation suggests that an additional phenomenon, in addition to the AF−FM transition, occurs for such high He^+ doses. One hypothesis to explain the exponential increase in current for large doses is that Fe near the surface is selectively sputtered, leaving behind a highly conductive Rh-rich alloy with electrical conductivity approaching that of pure Rh. This is supported by TRIM simulations in which 30 keV He^+ irradiation of FeRh sputters Fe at a 28% greater rate than Rh. At a dose of 10^{16} He^+ cm^{-2}, the surface would contain about 1.1×10^{14} more Rh at the surface. In comparison to the CAFM current map, the height map in Figure 5c reveals minimal changes for the lowest five doses in the bottom row, a slight increase in height for the second row and the first three features of the top row, and a slight reduction in height for the two highest He^+ doses. This lack of correlation between height and dose helps to rule out incremental carbon deposition as the source of spatially varying CAFM current. Based on these results, we believe that CAFM is a useful tool for verifying the size and shape of nanoscale He^+ direct-write patterns in FeRh films, and may also have some sensitivity toward identifying regions with a reduced metamagnetic transition temperature, particularly for He^+ doses $<3.6 \times 10^{15}$ He^+ cm^{-2}.

CAFM current and height images shown in Figure 5d,e illustrate the direct write capability of patterning well-resolved features down to 50 nm with a 100 nm pitch. The dose imparted in these features corresponds to the highest dose from the height map in Figure 5a of 3.6×10^{16} He^+ cm^{-2}, and the slight depressions observed in the height map of Figure 5e correlate well with this dose. The spot array features of Figure 5f approach the resolution-limit of the HIM, where a total of 2×10^5 He^+ were implanted at each fixed-point within the array. This exposure corresponds to the same total number of ions implanted in a 25 nm × 25 nm square at a dose level of 3.6×10^{16} He^+ cm^{-2} (see Methods and Figure S6). A spot array with a lower dose would likely achieve smaller feature sizes. The elongation of the features likely stems from beam astigmatism, but could also result from beam drift during the >30 ms dwell time at each spot. Like the other patterns, it shows an enhanced CAFM current and features with a lateral extent of 25 nm or less for some spots. This dose is likely just below the threshold for full amorphization,[58] yet is exceedingly large and leads to additional pitting of the FeRh film as shown in the AFM height map in Figure S6. Notwithstanding, the contrast in the CAFM is apparent, and the ability to pattern 25 nm regions or less supports the potential of patterning features to dimensions at or below the superparamagnetic limit by means of exchange coupling of the FM region to the AF matrix surrounding the feature.

Density Functional Theory. Collectively, our MOKE, CAFM, and optical microscopy measurements on the irradiated FeRh sample all indicate that the FM phase is present at temperatures well below the transition temperature of the pristine material. To understand the fundamental origins of why defects in FeRh can lower the transition temperature, we turn to first-principles calculations. The lattice parameter and magnetic moment on Fe and Rh in the FM and the AF phase of the FeRh cubic unit cell obtained from our first-principles calculations are summarized in Table 1.

https://dx.doi.org/10.1021/acsami.0c13565
ACS Appl. Mater. Interfaces 2021, 13, 836−847

Table 1. Lattice Parameter, a, and Magnitude of the Magnetic Moment on the Fe, m_{Fe}, and Rh, m_{Rh}, Atoms in the Cubic FeRh Structure with FM and AF Order Imposed Obtained from Our First-Principles Calculations[a]

	a (Å)	m_{Fe} (μB)	m_{Rh} (μB)
FM	3.017	3.34	1.01
FM (experiment)[59,60]	2.996	3.14	1.00
AF	3.003	3.32	0
AF (experiment)[59,60]	2.987	3.30	0

[a]Experimental data reported in refs[59,60] have been included for comparison. Static lattice first-principles calculations do not include thermal effects, such as lattice expansion, and thus yield differences between theory and experimental values.

In experiment, transitioning from the AF phase to the FM phase leads to a volume expansion of ~1%,[59] consistent with our first-principles calculations. This is accompanied by a change in the magnetic moment of the Rh atom and the direction of the Fe moments. In the AF phase, the magnetic moments on Fe are antiferromagnetically aligned along the axes of the cubic cell and are ferromagnetically aligned within the [111] plane, while Rh has no magnetic moment by symmetry. In the FM phase, the moments on Fe are aligned parallel to each other and Rh gains a magnetic moment of ~1 μB.

As in any first-order phase transition, the temperature T_m at which FeRh transitions between the AF and FM phase is determined by the tradeoff between the energy and entropy differences of the two phases. The free energies of the two phases are equal at the transition temperature, so

$$\Delta G = \Delta E(T_m) + P\Delta V(T_m) - T_m\Delta S(T_m) = 0$$

where ΔE is the energy difference, P is the pressure, ΔV is the volume difference, and ΔS is the entropy difference. The enthalpy contribution of the volume difference is negligible for a process involving rigid solids taking place at ambient pressure. The energy difference results from the structural energy associated with the change in volume and from changes in the direction and the magnitude of the magnetic moment on Fe and Rh. If we assume that the entropy difference is approximately independent of the presence of defects, then the energy difference and its variation with defects is, to a good approximation, proportional to the transition temperature and, therefore, its corresponding variation.[33,61,62]

From our first-principles calculations, the difference in total energy between the AF and the FM FeRh structure, which we call the spin-flip energy, is $\Delta E = E_{tot}(AF) - E_{tot}(FM)$, where $E_{tot}(AF)$ is the total energy of the FeRh structure with AF magnetic ordering and $E_{tot}(FM)$ is the total energy of the FeRh structure with FM magnetic ordering. We allow for a full relaxation of the atomic coordinates, volume, and cell shape for each magnetic configuration and find $\Delta E = -24.9$ meV/atom. The FM state is higher in energy, hence unstable at zero temperature, but becomes stable at finite temperature T_m because of the entropic effects. External perturbations such as strain, pressure, and defects would shift the energy balance between these two states, which would be reflected by a change in ΔE, and in turn the transition temperature. Hence, an analysis of the direction and magnitude of the shift in the transition temperature needs to consider changes in the volume and magnetic order on the Fe and Rh atoms.

If their lattice constants were epitaxially matched to that of MgO, the FM and AF configurations of FeRh would be under compressive in-plane biaxial strain, although it is likely that the strain in the 200 nm thick film relaxes far from the interface. The MgO lattice parameter from our first-principles calculations is 4.245 Å, which is close to the experimental MgO lattice parameter of 4.212 Å.[63] To determine the impact this maximum epitaxial strain would have on the spin-flip energy, we calculate ΔE imposing biaxial strain on the in-plane FeRh lattice parameters following the approach detailed in the Methods section. The results are illustrated in Figure 6a. The AF configuration remains lower in energy compared to the FM configuration for all values of the in-plane lattice parameter that we consider, that is, ΔE remains negative. An increase in the magnitude of ΔE corresponds to an increase in the energy to transition from the AF to the FM state. It is evident that when the in-plane lattice parameters of FeRh are strained to the MgO lattice, the magnitude of ΔE increases by 4% with respect to ΔE^{bulk}, which would correspond to an increase in the transition temperature with respect to the bulk transition temperature.

The main effect of the He^+ irradiation is the displacement of atoms, leading to localized disorder, forming over 200 vacancies per ion before coming to rest deep within the

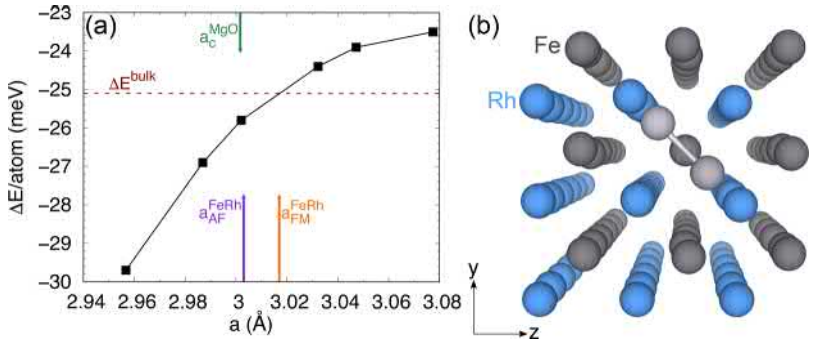

Figure 6. (a) Spin-flip energy [$\Delta E = E_{tot}(AF) - E_{tot}(FM)$] per atom between the AF and FM phases of FeRh as a function of equibiaxial in plane strain. The horizontal axis corresponds to the in-plane lattice parameters ($a = b$) that FeRh is fixed to in our calculations. The green, orange, and purple arrows correspond to the equilibrium lattice parameter of MgO (converted to cubic), cubic FM FeRh, and cubic AF FeRh obtained from our first-principles calculations. The horizontal red-dashed line, ΔE^{bulk}, denotes the equilibrium spin-flip energy using the fully relaxed AF and FM lattice parameters of the cubic FeRh cell. (b) Structure of the Fe split interstitial (light gray spheres) of the Fe Frenkel defect. Rh is depicted with blue spheres and Fe with gray spheres.

https://dx.doi.org/10.1021/acsami.0c13565
ACS Appl. Mater. Interfaces 2021, 13, 836−847

FeRh film, or in some cases passing entirely through the FeRh layer and coming to rest in the MgO substrate.[51] These displaced atoms will initially leave behind vacancies and move into interstitial positions, but preserve the stoichiometry. They may remain in this form as Frenkel pairs, heal completely by the annihilation of an interstitial with a vacancy of the same species, or create antisites by the recombination of an interstitial of one species with a vacancy of the other species. Prior first-principles calculations have suggested that defects may lower the transition temperature, assuming the transition temperature is proportional to the energy difference between the FM and AFM state. This was based on calculations of a single Fe and Rh antisite pair in a 16 atom FeRh cell (i.e., a concentration of 12.5% per formula unit), where they found the ground state to be FM.[64] Here, we simulate three types of point-defect pairs that preserve stoichiometry: Rh and Fe Frenkel pairs, and an antisite pair. We use large 432 atom supercells, which enables us to simulate defect concentrations (i.e., 1.17×10^{20} cm^{-3}) that are well below the defect concentration (i.e., 1.6×10^{22} cm^{-3}) that results in a saturated room-temperature Kerr rotation following He^+ irradiation.

The local structure around the defect controls its energy and magnetic structure, and therefore its effect on the transition temperature. While the vacancies and antisites induce only minor atomic relaxation, the interstitials lead to more drastic deformation of the lattice. To visualize one such defect, Figure 6b illustrates the atomic structure of the displaced Fe interstitial of the Fe Frenkel defect (Fe vacancy − interstitial pair). The Fe interstitial takes on a split-interstitial configuration, two Fe atoms sharing one Fe lattice site, with an Fe−Fe bond length of 2.03 Å. The Rh atoms that are nearest-neighbor to the Fe split-interstitial are displaced slightly outwards from their equilibrium positions. For the case of the Rh Frenkel pair (not shown), the displaced Rh interstitial does not form a split interstitial with a Rh atom within the lattice. Instead, it bonds to one of the Fe atoms, with a Fe−Rh bond length of 2.14 Å, resulting in the Fe atom being displaced away from its equilibrium position along the ⟨110⟩ direction. The Fe and Rh vacancies and antisites lead to minor changes in their nearest-neighbor bond lengths. For the case of Fe on the Rh antisite, the nearest neighbor Fe−Rh bond is 0.6% shorter than the equilibrium bond length while the Rh on the Fe antisite results in nearest-neighbor Rh−Fe bonds that are 3.3% shorter than the equilibrium bond length. The formation energies and percent change in spin flip energies are listed in Table 2.

Table 2. Point-Defect Pair Properties, Including Relaxed Formation Energies in the AF Order, and Change in Spin-Flip Energy Relative to Perfect Material at Concentration of One Pair Per 432 Atoms (1.7×10^{20} cm^{-3})[a]

defect	description	formation energy (eV)	spin-flip energy change (%)
$V_{Fe} - Fe_I$	Fe vacancy − interstitial pair	6.1	−3.3
$V_{Rh} - Rh_I$	Rh vacancy − interstitial pair	7.1	−2.74
Fe_{Rh}−Rh_{Fe}	Fe and Rh antisite defect pair	1.6	−5.5

[a]Formation energy calculations were terminated upon reaching a total energy convergence threshold of <1 μeV.

We found that the formation energies of the two types of Frenkel pairs in the AF order are quite large, about 6−7 eV, while the formation energy of an antisite pair is much lower, about 1.6 eV. If the system was in equilibrium, these energies would indicate that antisite defects would be much more abundant. Because the He^+ irradiation process is strongly out of equilibrium, this is not necessarily the case, but it does indicate that the driving force to heal vacancies and interstitials, whether back to the perfect lattice or to antisites, is strong. We also found that all types of defect pairs studied lower the magnitude of the spin flip energy by a few percent at the calculated concentration of two point-defects (one pair) per 432 atoms in the supercell (216 FeRh formula units per supercell). Within our approximation that the transition temperature is proportional to the spin flip energy, these results are consistent with the point defects reducing the transition temperature as seen experimentally.

CONCLUSIONS

In summary, we have established a direct-write process for tailoring the FeRh metamagnetic transition temperature using focused He^+ ion irradiation with spatial control down to 25 nm and approaching the superparamagnetic limit. Physical characterization of the material using HR-TEM and XRD confirms the crystalline quality and epitaxial registry with the MgO growth substrate. Our temperature-dependent MOKE images show a strong correlation between Kerr rotation and He^+ dose, directly confirming the tunability of the magnetic ordering from AF to FM with increasing temperature and lowering of the metamagnetic transition temperature with dose.

In this work, we introduce two characterization methods for indirectly quantifying the impact of He^+ irradiation on the metamagnetic transition of FeRh films. Foremost, temperature-dependent optical microscopy, with concomitant optical contrast image processing, is used to rapidly quantify the AF to FM transition for regions with varying dose. This technique correlates strongly with our temperature-dependent MOKE results, and reveals hysteresis in optical contrast for increasing and decreasing temperature sweeps—direct evidence of the metamagnetic transition. We employ CAFM as a means to characterize nanoscale features patterned in FeRh down to ∼25 nm. We begin with a dose-gradient array of squares that reveals a direct correlation of CAFM current magnitude with dose, while the topography shows a nonmonotonic trend providing evidence for the relationship between the CAFM current magnitude and the magnetic ordering of the FeRh film. These techniques, though very different in implementation, are fundamentally linked via the Hagen−Rubens relation where at optical frequencies, the coefficient of reflection is a function of the electrical conductivity.

We perform first principles-based calculations to quantify the impact that substrate strain and point defects (Frenkel and antisite pairs) have on the spin-flip energy of the system, which is directly related to the metamagnetic transition temperature. For FeRh grown on MgO, our calculations determine an increased magnitude of the spin-flip energy because of the epitaxial lattice-constant match, suggesting an increased metamagnetic transition temperature. In contrast, the simple defects we study here all lead to a slight reduction in the magnitude of the spin-flip energy. Therefore, no single defect type is responsible for modifying the metamagnetic transition,

https://dx.doi.org/10.1021/acsami.0c13565
ACS Appl. Mater. Interfaces 2021, 13, 836−847

but rather, any defect that degrades the AF ordering can play a role in decreasing the transition temperature.

Ultimately, our work demonstrates the ability to spatially pattern nanoscale magnetic ordering, as a gateway into realizing multiple domains of distinct magnetic ordering (AF, FM, and paramagnetic), on the same film. Our results thereby enable the creation of magnetic metamaterials and nanoscale interface-free AF spintronic devices that are dynamically temperature tunable.

METHODS

FeRh Thin Film Growth. For this study, we grew 200 nm thick epitaxial films of FeRh on single-crystal MgO(001) substrates using magnetron sputtering from a stoichiometric $Fe_{0.5}Rh_{0.5}$ target in a 5 mTorr Ar atmosphere. We fixed the substrate temperature at 630 °C during growth and performed a postgrowth anneal in 5 mTorr Ar for 1 h at 730 °C.

X-ray Analysis. We performed XRD to assess the initial crystalline quality of the films using the Cu Kα line of a Rigaku X-ray diffractometer with a rotating anode and the sample temperature cycled between 300 and 450 K.

TEM Preparation and Analysis. We employed an FEI Nova 600 NanoLab dual-beam, FIB (Ga)/scanning electron microscope system providing high-resolution ion milling and secondary electron-imaging capability to isolate and lift-out a thin foil of FeRh for subsequent TEM. Following lift-out, the foil was thinned and cleaned using the FIB with progressively lower accelerating voltages down to 2 kV. HRTEM images were collected using a JEOL JEM-2200FS at 200 kV and diffraction patterns were collected using a FEI Tecnai G2 at 300 kV.

Site-Selective He Ion Irradiation. Using a Zeiss ORION NanoFab helium ion microscope, we formed direct-write patterns consisting of a arrays of large area squares (20 μm × 20 μm) and small area squares ($\leq$2 μm × $\leq$2 μm) in FeRh films with 30 keV He^+ for subsequent characterization via optical and CAFM, respectively. In all cases, the irradiation was performed at normal incidence and controlled by the NanoFab Nanopatterning and Visualization Engine software, with the patterning direction along the x-axis leading to a y-axis raster direction. For larger regions, we used a 40 μm aperture, a 23.7 pA beam current, and a pixel spacing of 3.7 nm and varied the dwell time and number of replicates to achieve a wide-range of doses from 1×10^{14} to 8×10^{16} He^+ cm^{-2}. For smaller regions we used a 10 μm aperture, a 0.8 pA beam current, and a pixel spacing of 0.25 nm when applicable. Small scale features included a series of 2 μm × 2 μm uniformly dosed squares with doses ranging from 4.5×10^{13} to 3.6×10^{16} He^+ cm^{-2}, and arrays of nanoscale squares each filling a 2 μm × 2 μm area, with sizes/pitches of 200 nm/400 nm, 100 nm/200 nm, 50 nm/100 nm, and 25 nm/50 nm. Each nanoscale feature was dosed to the same level of 3.6×10^{16} He^+ cm^{-2} for an effective areal dose of 8.75×10^{15} He^+ cm^{-2} averaged over the 2 μm × 2 μm region. We chose this dose level to ensure the nanoscale features consist of fully saturated FM ordering. To push the ultimate scaling limits of the NanoFab, we patterned a spot array with a spot dose of 2×10^5 He^+ and a pitch of 50 nm, which has approximately the same total ions per region and pitch as the 25 nm/50 nm square pattern array. For these patterns, we optimized beam focus and aperture settings in a small region adjacent to the patterning region, then ensured proper positioning and beam focus by capturing a single large area exposure with a beam current of ~0.8 pA imparting a total dose less than 10^{11} He^+/cm^2.

Temperature-Dependent Optical Microscopy. Using a Nikon optical microscope and a LabVIEW controlled heated vacuum stage, we captured temperature-dependent optical microscopy images. Brightness and contrast remained constant for all images, and at each temperature we allowed the sample to equilibrate for >5 min prior to refocusing and capturing an image. Refocusing was unavoidable because of the thermal expansion of the stage and sample over the large temperature range investigated.

MOKE Imaging. We performed temperature-dependent longitudinal MOKE imaging and magnetization studies using a Quantum Design NanoMOKE3. A Montana cryostat extension was used for the measurements below room temperature and an Oxford cryostat was used for heating the sample above room temperature. The Kerr signal was taken using a 10 μm spot-size, which fits well within the 20 μm × 20 μm irradiated squares, and imaging was done by scanning the laser spot across the sample.

SQUID Magnetometry. We used a Quantum Design MPMS3 SQUID magnetometer equipped with a high-temperature oven to measure temperature-dependent DC magnetization from 300 to 500 K with a continuous sweep at a rate of 3 K/min in a 100 Oe magnetic field applied parallel to the plane of the film. The square-shaped sample had an area of 5 × 5 mm^2 and was mounted to the heater stick with a covering of high-temperature ZIRCAR cement and surrounded with a copper radiation shield.

Thin-Film Conductivity Measurements. We performed four probe van der Pauw conductance measurements using a modified advanced research systems probe station with programmed temperature cycling.

Conductive Atomic Force Microscopy. Using a Keysight 9500 AFM we performed CAFM measurements with nanocrystalline doped diamond coated cantilevers (BudgetSensors AIO-DD). During measurements, the sample chamber was continuously purged with nitrogen. Bias applied to the sample causes current to flow between the sample and tip, which is measured with a current amplifier attached to the tip.

Density Functional Theory. Our density functional theory calculations use the projector-augmented wave (PAW) method[65] as implemented in the VASP code[66] with the generalized gradient approximation defined by the Perdew–Burke–Ernzerhof[67] functional. We use the Fe and Rh PAW potentials that treat the s, p, and d states as valence, and a plane-wave energy cutoff of 400 eV. Structural relaxation of the lattice parameters and internal coordinates of the unit cell were carried out with a 12 × 12 × 12 k-point grid and a force convergence criterion of 5 meV $Å^{-1}$. To correctly describe the magnetic moments of Fe, we use a spherically averaged Hubbard correction within the fully localized limit double-counting subtraction.[68] We apply a $U-J$ value of 1 eV to the Fe d-states, which leads to a magnetic moment on Fe in the FM and AF phase that is in agreement with experiment.[59] To study the effects of biaxial strain, we performed "strained-bulk" calculations where we imposed compressive and tensile equibiaxial strain on the in-plane lattice parameters of the FeRh unit cell and optimized the out-of-plane lattice parameter and all atomic positions of the unit cell. Calculations on MgO used the same k-point grid, force convergence criterion, and a 600 eV plane-wave energy cutoff.

We carried out calculations of defects in FeRh using 6 × 6 × 6 supercells of the primitive cubic cell (432 atoms total), constructed using the lattice vectors of the fully optimized AF FeRh cubic unit cell. We examined defects that preserve the stoichiometry, namely Frenkel (same species vacancy and interstitial) pairs and antisite pairs. The positions of the two-point defects in each supercell were chosen to maximize their distance. We optimized the atomic coordinates of each defect configuration with FM and AF order imposed at a fixed volume and used Γ-point Brillouin zone sampling for the defect calculations. We also evaluated the energy difference between the two magnetic orders at the AF-relaxed positions.

ASSOCIATED CONTENT

Supporting Information

The Supporting Information is available free of charge at https://pubs.acs.org/doi/10.1021/acsami.0c13565.

Temperature-dependent XRD-extracted c-lattice parameter and crystallite size, AMF images of heavily implanted regions, TRIM-based vacancy generation He^+ profile, low-temperature MOKE images, temper-

https://dx.doi.org/10.1021/acsami.0c13565
ACS Appl. Mater. Interfaces 2021, 13, 836–847

ature-dependent optical contrast magnitude, and AFM height and the corresponding current maps (PDF)

AUTHOR INFORMATION

Corresponding Authors

Cory D. Cress − *Electronics Science and Technology Division, United States Naval Research Laboratory, Washington, DC 20375, United States;* orcid.org/0000-0001-7563-6693; Email: cory.cress@nrl.navy.mil

Steven P. Bennett − *Materials Science and Technology Division, United States Naval Research Laboratory, Washington, DC 20375, United States;* orcid.org/0000-0003-2615-6321; Email: steve.bennett@nrl.navy.mil

Authors

Darshana Wickramaratne − *NRC Postdoc Residing at the Materials Science and Technology Division, United States Naval Research Laboratory, Washington, DC 20375, United States;* orcid.org/0000-0002-1663-1507

Matthew R. Rosenberger − *Materials Science and Technology Division, United States Naval Research Laboratory, Washington, DC 20375, United States;* orcid.org/0000-0001-6866-5488

Zachariah Hennighausen − *NRC Postdoc Residing at the Materials Science and Technology Division, United States Naval Research Laboratory, Washington, DC 20375, United States;* orcid.org/0000-0001-5663-3331

Patrick G. Callahan − *Materials Science and Technology Division, United States Naval Research Laboratory, Washington, DC 20375, United States*

Samuel W. LaGasse − *NRC Postdoc Residing at the Electronics Science and Technology Division, United States Naval Research Laboratory, Washington, DC 20375, United States;* orcid.org/0000-0001-8739-9621

Noam Bernstein − *Materials Science and Technology Division, United States Naval Research Laboratory, Washington, DC 20375, United States;* orcid.org/0000-0002-6532-1337

Olaf M. van 't Erve − *Materials Science and Technology Division, United States Naval Research Laboratory, Washington, DC 20375, United States*

Berend T. Jonker − *Materials Science and Technology Division, United States Naval Research Laboratory, Washington, DC 20375, United States;* orcid.org/0000-0001-8816-7857

Syed B. Qadri − *Materials Science and Technology Division, United States Naval Research Laboratory, Washington, DC 20375, United States*

Joseph C. Prestigiacomo − *Materials Science and Technology Division, United States Naval Research Laboratory, Washington, DC 20375, United States;* orcid.org/0000-0001-5274-8836

Marc Currie − *Optical Sciences Division, United States Naval Research Laboratory, Washington, DC 20375, United States;* orcid.org/0000-0002-6139-6710

Igor I. Mazin − *Department of Physics and Astronomy and the Quantum Materials Center, George Mason University, Fairfax, Virginia 22030, United States;* orcid.org/0000-0001-9456-7099

Complete contact information is available at: https://pubs.acs.org/10.1021/acsami.0c13565

Author Contributions

C.D.C., S.P.B., and O.M.v.t.E. conceived of the study and provided project administration. C.D.C. performed HIM irradiation experiments, optical measurements, data analysis, and wrote the first draft with assistance from S.P.B. S.P.B. grew FeRh samples and performed temperature-dependent XRD measurements with assistance from S.B.Q. O.M.v.t.E. and Z.H. performed MOKE and transport measurements with assistance and resources contributed by B.T.J. J.C.P. performed SQUID magnetization measurements. M.R.R. performed CAFM measurements and analysis with assistance and resources contributed by B.T.J. M.C. performed optical analysis. D.W., N.B., and I.I.M. contributed the density functional theory simulations of defects. S.W.L. analyzed the optical microscopy measurements and performed AFM. P.G.C. conducted the TEM analysis. All authors discussed the results and contributed to editing the manuscript.

Notes

The authors declare no competing financial interest.

ACKNOWLEDGMENTS

We acknowledge financial support of this research from the Office of Naval Research 6.1 Base Funding. S.W.L., D.W., and Z.H. held National Research Council Associateship Awards at the Naval Research Laboratory. We thank D. Kidwell for assistance with HIM.

REFERENCES

(1) Okuno, T.; Kim, D.-H.; Oh, S.-H.; Kim, S. K.; Hirata, Y.; Nishimura, T.; Ham, W. S.; Futakawa, Y.; Yoshikawa, H.; Tsukamoto, A.; Tserkovnyak, Y.; Shiota, Y.; Moriyama, T.; Kim, K.-J.; Lee, K.-J.; Ono, T. Spin-Transfer Torques for Domain Wall Motion in Antiferromagnetically Coupled Ferrimagnets. *Nat. Electron.* **2019**, *2*, 389−393.

(2) Liu, Z.; Feng, Z.; Yan, H.; Wang, X.; Zhou, X.; Qin, P.; Guo, H.; Yu, R.; Jiang, C. Antiferromagnetic Piezospintronics. *Adv. Electron. Mater.* **2019**, *5*, 1900176.

(3) Jungwirth, T.; Sinova, J.; Manchon, A.; Marti, X.; Wunderlich, J.; Felser, C. The Multiple Directions of Antiferromagnetic Spintronics. *Nat. Phys.* **2018**, *14*, 200−203.

(4) Němec, P.; Fiebig, M.; Kampfrath, T.; Kimel, A. V. Antiferromagnetic Opto-Spintronics. *Nat. Phys.* **2018**, *14*, 229−241.

(5) Liu, Z. Q.; Li, L.; Gai, Z.; Clarkson, J. D.; Hsu, S. L.; Wong, A. T.; Fan, L. S.; Lin, M.-W.; Rouleau, C. M.; Ward, T. Z.; Lee, H. N.; Sefat, A. S.; Christen, H. M.; Ramesh, R. Full Electroresistance Modulation in a Mixed-Phase Metallic Alloy. *Phys. Rev. Lett.* **2016**, *116*, 097203.

(6) Heron, J. T.; Bosse, J. L.; He, Q.; Gao, Y.; Trassin, M.; Ye, L.; Clarkson, J. D.; Wang, C.; Liu, J.; Salahuddin, S.; Ralph, D. C.; Schlom, D. G.; Íñiguez, J.; Huey, B. D.; Ramesh, R. Deterministic Switching of Ferromagnetism at Room Temperature Using an Electric Field. *Nature* **2014**, *516*, 370−373.

(7) Causer, G. L.; Cortie, D. L.; Zhu, H.; Ionescu, M.; Mankey, G. J.; Wang, X. L.; Klose, F. Direct Measurement of the Intrinsic Sharpness of Magnetic Interfaces Formed by Chemical Disorder Using a He + Beam. *ACS Appl. Mater. Interfaces* **2018**, *10*, 16216−16224.

(8) Bennett, S. P.; Herklotz, A.; Cress, C. D.; Ievlev, A.; Rouleau, C. M.; Mazin, I. I.; Lauter, V. Magnetic Order Multilayering in FeRh Thin Films by He-Ion Irradiation. *Mater. Res. Lett.* **2018**, *6*, 106−112.

(9) Ehrler, J.; He, M.; Shugaev, M. V.; Polushkin, N. I.; Wintz, S.; Liersch, V.; Cornelius, S.; Hübner, R.; Potzger, K.; Lindner, J.; Fassbender, J.; Ünal, A. A.; Valencia, S.; Kronast, F.; Zhigilei, L. V.; Bali, R. Laser-Rewriteable Ferromagnetism at Thin-Film Surfaces. *ACS Appl. Mater. Interfaces* **2018**, *10*, 15232−15239.

(10) Fina, I.; Quintana, A.; Padilla-Pantoja, J.; Martí, X.; Macià, F.; Sánchez, F.; Foerster, M.; Aballe, L.; Fontcuberta, J.; Sort, J. Electric-

Field-Adjustable Time-Dependent Magnetoelectric Response in Martensitic FeRh Alloy. *ACS Appl. Mater. Interfaces* **2017**, *9*, 15577−15582.
(11) Mei, A. B.; Gray, I.; Tang, Y.; Schubert, J.; Werder, D.; Bartell, J.; Ralph, D. C.; Fuchs, G. D.; Schlom, D. G. Local Photothermal Control of Phase Transitions for On-Demand Room-Temperature Rewritable Magnetic Patterning. *Adv. Mater.* **2020**, *32*, 2001080.
(12) Massey, J. R.; Matsumoto, K.; Strungaru, M.; Temple, R. C.; Higo, T.; Kondou, K.; Evans, R. F. L.; Burnell, G.; Chantrell, R. W.; Otani, Y.; Marrows, C. H. Phase Boundary Exchange Coupling in the Mixed Magnetic Phase Regime of a Pd-Doped FeRh Epilayer. *Phys. Rev. Mater.* **2020**, *4*, 024403.
(13) Lommel, J. M.; Kouvel, J. S. Effects of Mechanical and Thermal Treatment on the Structure and Magnetic Transitions in FeRh. *J. Appl. Phys.* **1967**, *38*, 1263−1264.
(14) Jacobs, I. S.; Lawrence, P. E. Metamagnetic Phase Transitions and Hysteresis in FeCl2. *Phys. Rev.* **1967**, *164*, 866−878.
(15) Lyubina, J.; Gutfleisch, O.; Kuz'min, M. D.; Richter, M. La(Fe,Si)13-Based Magnetic Refrigerants Obtained by Novel Processing Routes. *J. Magn. Magn. Mater.* **2008**, *320*, 2252−2258.
(16) Aeppli, G.; Bucher, E.; Broholm, C.; Kjems, J. K.; Baumann, J.; Hufnagl, J. Magnetic Order and Fluctuations in Superconducting UPt3. *Phys. Rev. Lett.* **1988**, *60*, 615−618.
(17) Zhang, S.-y.; Zhao, P.; Li, R.-w.; Zhang, H.-w.; Shen, B.-g. Antiferro- to Ferromagnetic Transition and Large Magnetoresistance in YMn6Sn6−xTix (X=0−1.0) Compounds. *J. Appl. Phys.* **2002**, *91*, 5250−5253.
(18) Kouvel, J. S. Unusual Nature of the Abrupt Magnetic Transition in FeRh and Its Pseudobinary Variants. *J. Appl. Phys.* **1966**, *37*, 1257−1258.
(19) Kouvel, J. S.; Hartelius, C. C. Anomalous Magnetic Moments and Transformations in the Ordered Alloy FeRh. *J. Appl. Phys.* **1962**, *33*, 1343−1344.
(20) Feng, Z.; Yan, H.; Liu, Z. Electric-Field Control of Magnetic Order: From FeRh to Topological Antiferromagnetic Spintronics. *Adv. Electron. Mater.* **2019**, *5*, 1800466.
(21) Vogler, C.; Abert, C.; Bruckner, F.; Suess, D. Noise Reduction Based on an Fe-Rh Interlayer in Exchange-Coupled Heat-Assisted Recording Media. *Phys. Rev. Appl.* **2017**, *8*, 054021.
(22) Uhlíř, V.; Arregi, J. A.; Fullerton, E. E. Colossal Magnetic Phase Transition Asymmetry in Mesoscale FeRh Stripes. *Nat. Commun.* **2016**, *7*, 13113.
(23) Gray, I.; Stiehl, G. M.; Heron, J. T.; Mei, A. B.; Schlom, D. G.; Ramesh, R.; Ralph, D. C.; Fuchs, G. D. Imaging Uncompensated Moments and Exchange-Biased Emergent Ferromagnetism in FeRh Thin Films. *Phys. Rev. Mater.* **2019**, *3*, 124407.
(24) Liu, Y.; Phillips, L. C.; Mattana, R.; Bibes, M.; Barthélémy, A.; Dkhil, B. Large Reversible Caloric Effect in FeRh Thin Films via a Dual-Stimulus Multicaloric Cycle. *Nat. Commun.* **2016**, *7*, 11614.
(25) Cherifi, R. O.; Ivanovskaya, V.; Phillips, L. C.; Zobelli, A.; Infante, I. C.; Jacquet, E.; Garcia, V.; Fusil, S.; Briddon, P. R.; Guiblin, N.; Mougin, A.; Ünal, A. A.; Kronast, F.; Valencia, S.; Dkhil, B.; Barthélémy, A.; Bibes, M. Electric-Field Control of Magnetic Order above Room Temperature. *Nat. Mater.* **2014**, *13*, 345−351.
(26) Bennett, S. P.; Wong, A. T.; Glavic, A.; Herklotz, A.; Urban, C.; Valmianski, I.; Biegalski, M. D.; Christen, H. M.; Ward, T. Z.; Lauter, V. Giant Controllable Magnetization Changes Induced by Structural Phase Transitions in a Metamagnetic Artificial Multiferroic. *Sci. Rep.* **2016**, *6*, 22708.
(27) Warren, J. L.; Barton, C. W.; Bull, C.; Thomson, T. Topography Dependence of the Metamagnetic Phase Transition in FeRh Thin Films. *Sci. Rep.* **2020**, *10*, 4030.
(28) Witte, R.; Kruk, R.; Wang, D.; Schlabach, S.; Brand, R. A.; Gruner, M. E.; Wende, H.; Hahn, H. Epitaxial Strain Adaptation in Chemically Disordered FeRh Thin Films. *Phys. Rev. B* **2019**, *99*, 134109.
(29) Urban, C.; Bennett, S. P.; Schuller, I. K. Hydrostatic Pressure Mapping of Barium Titanate Phase Transitions with Quenched FeRh. *Sci. Rep.* **2020**, *10*, 6312.
(30) Pressacco, F.; Uhlíř, V.; Gatti, M.; Nicolaou, A.; Bendounan, A.; Arregi, J. A.; Patel, S. K. K.; Fullerton, E. E.; Krizmancic, D.; Sirotti, F. Laser Induced Phase Transition in Epitaxial FeRh Layers Studied by Pump-Probe Valence Band Photoemission. *Struct. Dyn.* **2018**, *5*, 034501.
(31) McGrath, B. R.; Camley, R. E.; Livesey, K. L. Self-Consistent Local Mean-Field Theory for Phase Transitions and Magnetic Properties of FeRh. *Phys. Rev. B* **2020**, *101*, 014444.
(32) Aschauer, U.; Braddell, R.; Brechbühl, S. A.; Derlet, P. M.; Spaldin, N. A. Strain-Induced Structural Instability in FeRh. *Phys. Rev. B* **2016**, *94*, 014109.
(33) Wolloch, M.; Gruner, M. E.; Keune, W.; Mohn, P.; Redinger, J.; Hofer, F.; Suess, D.; Podloucky, R.; Landers, J.; Salamon, S.; Scheibel, F.; Spoddig, D.; Witte, R.; Cuenya, B. R.; Gutfleisch, O.; Hu, M. Y.; Zhao, J.; Toellner, T.; Alp, E. E.; Siewert, M.; Entel, P.; Pentcheva, R.; Wende, H. Impact of Lattice Dynamics on the Phase Stability of Metamagnetic FeRh: Bulk and Thin Films. *Phys. Rev. B* **2016**, *94*, 174435.
(34) Kudrnovský, J.; Drchal, V.; Turek, I. Physical Properties of FeRh Alloys: The Antiferromagnetic to Ferromagnetic Transition. *Phys. Rev. B: Condens. Matter Mater. Phys.* **2015**, *91*, 014435.
(35) Lewis, L. H.; Marrows, C. H.; Langridge, S. Coupled Magnetic, Structural, and Electronic Phase Transitions in FeRh. *J. Phys. D: Appl. Phys.* **2016**, *49*, 323002.
(36) Baranov, N. V.; Barabanova, E. A. Electrical Resistivity and Magnetic Phase Transitions in Modified FeRh Compounds. *J. Alloys Compd.* **1995**, *219*, 139−148.
(37) Barua, R.; Jiménez-Villacorta, F.; Lewis, L. H. Predicting Magnetostructural Trends in FeRh-Based Ternary Systems. *Appl. Phys. Lett.* **2013**, *103*, 102407.
(38) Soma, R.; Saitoh, Y.; Sakamaki, M.; Amemiya, K.; Iwase, A.; Matsui, T. Irradiation Effect on Magnetic Properties of FeRh Thin Films with Energetic C60 Cluster Ion Beam. *AIP Adv.* **2018**, *8*, 056433.
(39) Fujita, N.; Matsui, T.; Kosugi, S.; Satoh, T.; Saitoh, Y.; Takano, K.; Koka, M.; Kamiya, T.; Seki, S.; Iwase, A. Micrometer-Sized Magnetic Patterning of FeRh Films Using an Energetic Ion Microbeam. *Jpn. J. Appl. Phys.* **2010**, *49*, 060211.
(40) Bali, R.; Wintz, S.; Meutzner, F.; Hübner, R.; Boucher, R.; Ünal, A. A.; Valencia, S.; Neudert, A.; Potzger, K.; Bauch, J.; Kronast, F.; Facsko, S.; Lindner, J.; Fassbender, J. Printing Nearly-Discrete Magnetic Patterns Using Chemical Disorder Induced Ferromagnetism. *Nano Lett.* **2014**, *14*, 435−441.
(41) Mougin, A.; Mewes, T.; Jung, M.; Engel, D.; Ehresmann, A.; Schmoranzer, H.; Fassbender, J.; Hillebrands, B. Local Manipulation and Reversal of the Exchange Bias Field by Ion Irradiation in FeNi/FeMn Double Layers. *Phys. Rev. B: Condens. Matter Mater. Phys.* **2001**, *63*, 060409.
(42) Cervera, S.; Trassinelli, M.; Marangolo, M.; Carrétéro, C.; Garcia, V.; Hidki, S.; Jacquet, E.; Lamour, E.; Lévy, A.; Macé, S.; Prigent, C.; Rozet, J. P.; Steydli, S.; Vernhet, D. Modulating the Phase Transition Temperature of Giant Magnetocaloric Thin Films by Ion Irradiation. *Phys. Rev. Mater.* **2017**, *1*, 065402.
(43) Fujita, N.; Kosugi, S.; Saitoh, Y.; Kaneta, Y.; Kume, K.; Batchuluun, T.; Ishikawa, N.; Matsui, T.; Iwase, A. Magnetic States Controlled by Energetic Ion Irradiation in FeRh Thin Films. *J. Appl. Phys.* **2010**, *107*, 09E302.
(44) Heidarian, A.; Bali, R.; Grenzer, J.; Wilhelm, R. A.; Heller, R.; Yildirim, O.; Lindner, J.; Potzger, K. Tuning the Antiferromagnetic to Ferromagnetic Phase Transition in FeRh Thin Films by Means of Low-Energy/Low Fluence Ion Irradiation. *Nucl. Instrum. Methods Phys. Res., Sect. B* **2015**, *358*, 251−254.
(45) Koide, T.; Satoh, T.; Kohka, M.; Saitoh, Y.; Kamiya, T.; Ohkouchi, T.; Kotsugi, M.; Kinoshita, T.; Nakamura, T.; Iwase, A.; Matsui, T. Magnetic Patterning of FeRh Thin Films by Energetic Light Ion Microbeam Irradiation. *Jpn. J. Appl. Phys.* **2014**, *53*, 05FC06.
(46) Allen, F. I.; Velez, N. R.; Thayer, R. C.; Patel, N. H.; Jones, M. A.; Meyers, G. F.; Minor, A. M. Gallium, Neon and Helium Focused

Ion Beam Milling of Thin Films Demonstrated for Polymeric Materials: Study of Implantation Artifacts. *Nanoscale* **2019**, *11*, 1403−1409.
(47) Allen, F. I.; Hosemann, P.; Balooch, M. Key Mechanistic Features of Swelling and Blistering of Helium-Ion-Irradiated Tungsten. *Scr. Mater.* **2020**, *178*, 256−260.
(48) Klein, J.; Kuc, A.; Nolinder, A.; Altzschner, M.; Wierzbowski, J.; Sigger, F.; Kreupl, F.; Finley, J. J.; Wurstbauer, U.; Holleitner, A. W.; Kaniber, M. Robust Valley Polarization of Helium Ion Modified Atomically Thin MoS 2. *2D Mater.* **2017**, *5*, 011007.
(49) Klein, J.; Lorke, M.; Florian, M.; Sigger, F.; Sigl, L.; Rey, S.; Wierzbowski, J.; Cerne, J.; Müller, K.; Mitterreiter, E.; Zimmermann, P.; Taniguchi, T.; Watanabe, K.; Wurstbauer, U.; Kaniber, M.; Knap, M.; Schmidt, R.; Finley, J. J.; Holleitner, A. W. Site-Selectively Generated Photon Emitters in Monolayer MoS2 via Local Helium Ion Irradiation. *Nat. Commun.* **2019**, *10*, 2755.
(50) Hlawacek, G. Ion Microscopy. In *Springer Handbook of Microscopy*; Hawkes, P. W., Spence, J. C. H., Eds.; Springer International Publishing: Cham, 2019; pp 677−714.
(51) Ziegler, J. F.; Ziegler, M. D.; Biersack, J. P. SRIM − The Stopping and Range of Ions in Matter. *Nucl. Instrum. Methods Phys. Res., Sect. B* **2010**, *268*, 1818−1823.
(52) Boschini, M. J.; Rancoita, P. G.; Tacconi, M. SR-NIEL Calculator: Screened Relativistic (SR) Treatment for Calculating the Displacement Damage and Nuclear Stopping Powers for Electrons, Protons, Light- and Heavy- Ions in Materials (version 6.2.4). http://www.sr-niel.org (accessed Jan 17, 2020).
(53) Eggert, B.; Schmeink, A.; Lill, J.; Liedke, M. O.; Kentsch, U.; Butterling, M.; Wagner, A.; Pascarelli, S.; Potzger, K.; Lindner, J.; Thomson, T.; Fassbender, J.; Ollefs, K.; Keune, W.; Bali, R.; Wende, H. Magnetic Response of FeRh to Static and Dynamic Disorder. *RSC Adv.* **2020**, *10*, 14386−14395.
(54) Ehrler, J.; Sanyal, B.; Grenzer, J.; Zhou, S.; Boettger, R.; Eggert, B.; Wende, H.; Lindner, J.; Fassbender, J.; Leyens, C.; Potzger, K.; Bali, R. Magneto-Structural Correlations in a Systematically Disordered B2 Lattice. *New J. Phys.* **2020**, *22*, 073004.
(55) Iwase, A.; Fukuzumi, M.; Zushi, Y.; Suzuki, M.; Takagaki, M.; Kawamura, N.; Chimi, Y.; Ishikawa, N.; Mizuki, J.; Ono, F. Study on Irradiation-Induced Magnetic Transition in FeRh Alloys by Means of Fe K-Edge XMCD Spectroscopy. *Nucl. Instrum. Methods Phys. Res., Sect. B* **2007**, *256*, 429−433.
(56) Arregi, J. A.; Horký, M.; Fabianová, K.; Tolley, R.; Fullerton, E. E.; Uhlíř, V. Magnetization Reversal and Confinement Effects across the Metamagnetic Phase Transition in Mesoscale FeRh Structures. *J. Phys. D: Appl. Phys.* **2018**, *51*, 105001.
(57) Bennett, S. P.; Currie, M.; van't Erve, O. M. J.; Mazin, I. I. Spectral Reflectivity Crossover at the Metamagnetic Transition in FeRh Thin Films. *Opt. Mater. Express* **2019**, *9*, 2870.
(58) Livengood, R.; Tan, S.; Greenzweig, Y.; Notte, J.; McVey, S. Subsurface Damage from Helium Ions as a Function of Dose, Beam Energy, and Dose Rate. *J. Vac. Sci. Technol., B: Microelectron. Nanometer Struct.–Process., Meas., Phenom.* **2009**, *27*, 3244.
(59) Shirane, G.; Nathans, R.; Chen, C. W. Magnetic Moments and Unpaired Spin Densities in the Fe-Rh Alloys. *Phys. Rev.* **1964**, *134*, A1547−A1553.
(60) Zakharov, A. I.; Kadomtseva, A. M.; Levitin, R. Z.; Ponyatovskii, E. G. Magnetic and Magnetoelastic Properties of a Metamagnetic Iron-rhodium Alloy. *J. Exp. Theor. Phys.* **1964**, *19*, 1348.
(61) Zarkevich, N. A.; Johnson, D. D. FeRh Ground State and Martensitic Transformation. *Phys. Rev. B* **2018**, *97*, 014202.
(62) Zarkevich, N. A.; Johnson, D. D. Reliable Thermodynamic Estimators for Screening Caloric Materials. *J. Alloys Compd.* **2019**, *802*, 712−722.
(63) Isaak, D. G.; Anderson, O. L.; Goto, T. Measured Elastic Moduli of Single-Crystal MgO up to 1800 K. *Phys. Chem. Miner.* **1989**, *16*, 704−713.
(64) Kaneta, Y.; Ishino, S.; Chen, Y.; Iwata, S.; Iwase, A. Theoretical Calculations for Magnetic Property of FeRh Inter-Metallic Compound with Site-Exchange Defects. *Jpn. J. Appl. Phys.* **2011**, *50*, 105803.
(65) Blöchl, P. E. Projector Augmented-Wave Method. *Phys. Rev. B: Condens. Matter Mater. Phys.* **1994**, *50*, 17953−17979.
(66) Kresse, G.; Hafner, J. Ab Initio Molecular Dynamics for Liquid Metals. *Phys. Rev. B: Condens. Matter Mater. Phys.* **1993**, *47*, 558−561.
(67) Perdew, J. P.; Burke, K.; Ernzerhof, M. Generalized Gradient Approximation Made Simple. *Phys. Rev. Lett.* **1996**, *77*, 3865−3868.
(68) Anisimov, V. I.; Solovyev, I. V.; Korotin, M. A.; Czyżyk, M. T.; Sawatzky, G. A. Density-Functional Theory and NiO Photoemission Spectra. *Phys. Rev. B: Condens. Matter Mater. Phys.* **1993**, *48*, 16929−16934.

https://dx.doi.org/10.1021/acsami.0c13565
ACS Appl. Mater. Interfaces 2021, 13, 836−847

Direct-Write of Nanoscale Domains with Tunable Metamagnetic Order in FeRh Thin Films

Cory D. Cress[1*], Darshana Wickramaratne[2], Matthew R. Rosenberger[3], Zachariah Hennighausen[2], Patrick G. Callahan[3], Samuel W. LaGasse[4], Noam Bernstein[3], Olaf M. van 't Erve[3], Berend T. Jonker[3], Syed B. Qadri[3], Joseph C. Prestigiacomo[3], Marc Currie[5], Igor I. Mazin[6], and Steven P. Bennett[3*]

[1]*Electronics Science and Technology Division, United States Naval Research Laboratory, Washington DC 20375, USA*

[2]*NRC Postdoc Residing at the Materials Science and Technology Division, United States Naval Research Laboratory, Washington DC 20375, USA*

[3]*Materials Science and Technology Division, United States Naval Research Laboratory, Washington DC 20375, USA*

[4]*NRC Postdoc Residing at the Electronics Science and Technology Division, United States Naval Research Laboratory, Washington DC 20375, USA*

[5]*Optical Sciences Division, United States Naval Research Laboratory, Washington DC 20375, USA*

[6]*Department of Physics and Astronomy and the Quantum Materials Center, George Mason University, Fairfax VA 22030, USA*

*Corresponding Authors: cory.cress@nrl.navy.mil, steve.bennett@nrl.navy.mil

In Figure S1 we show lattice parameter results from XRD as a function of temperature while cooling and heating through the transition. The lattice parameter was obtained by fitting the 003 peak shown in Figure 1(a) of the main text to a Gaussian and plotting the centroid. FWHM was also extracted from the Gaussian fits and converted to a crystallite size using the Scherrer equation and plotted as a function of temperature to show overall volume expansion of the FeRh lattice through the metamagnetic transition.

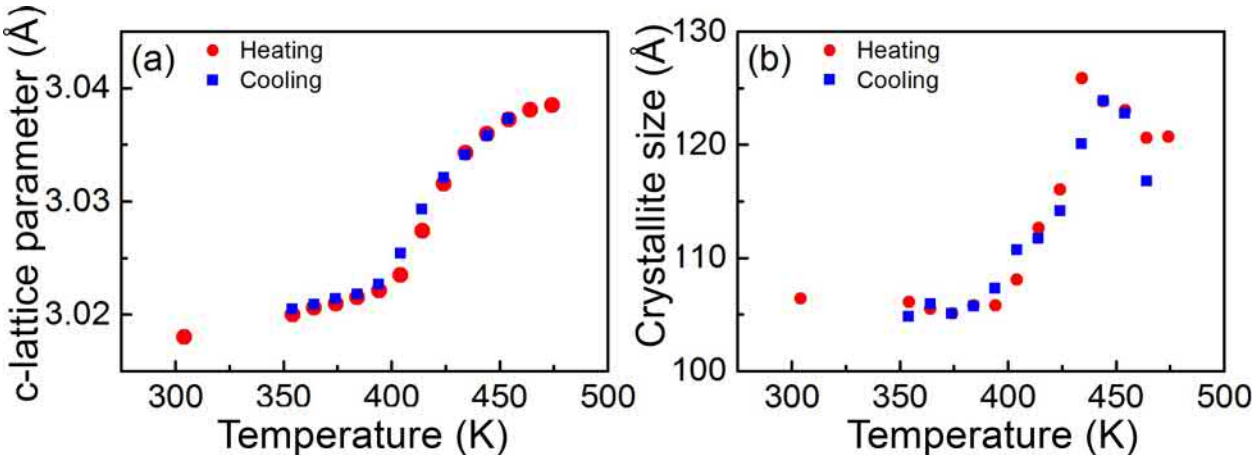

Figure S1. (a) Lattice parameter extracted from XRD of the 003 peak shown in Figure 1(a) of the main text as a function of temperature. (b) Crystallite size calculated by the Scherrer equation from the FWHM of the 003 peak as a function of temperature.

In Figure S2 we show a series of four AFMs taken for 4 different doses corresponding to the lowest and highest investigated in this study. Boxes 1-3 are in the regime of the lowest doses investigated in this work. In Box 1 and Box 2 a small increase in height is observed near the corner of the box whereas Box 3, the lowest dose, has no observable deviation. In contrast, the highest dose of ~8×10^{16} He^{+}/cm^{2}, which exceeds all doses in this study, contains a region of apparent carbon deposition of ~12 nm that is confined to the edge of the feature. Despite the lack of a height variation near the center of Box 10, we observe a clear contrast in the micrograph indicating that

carbon deposition alone is not responsible for the changes we observe in the helium ion micrographs. Based on AFM micrograph analysis, the as-grown film RMS roughness is ≤1.5 nm.

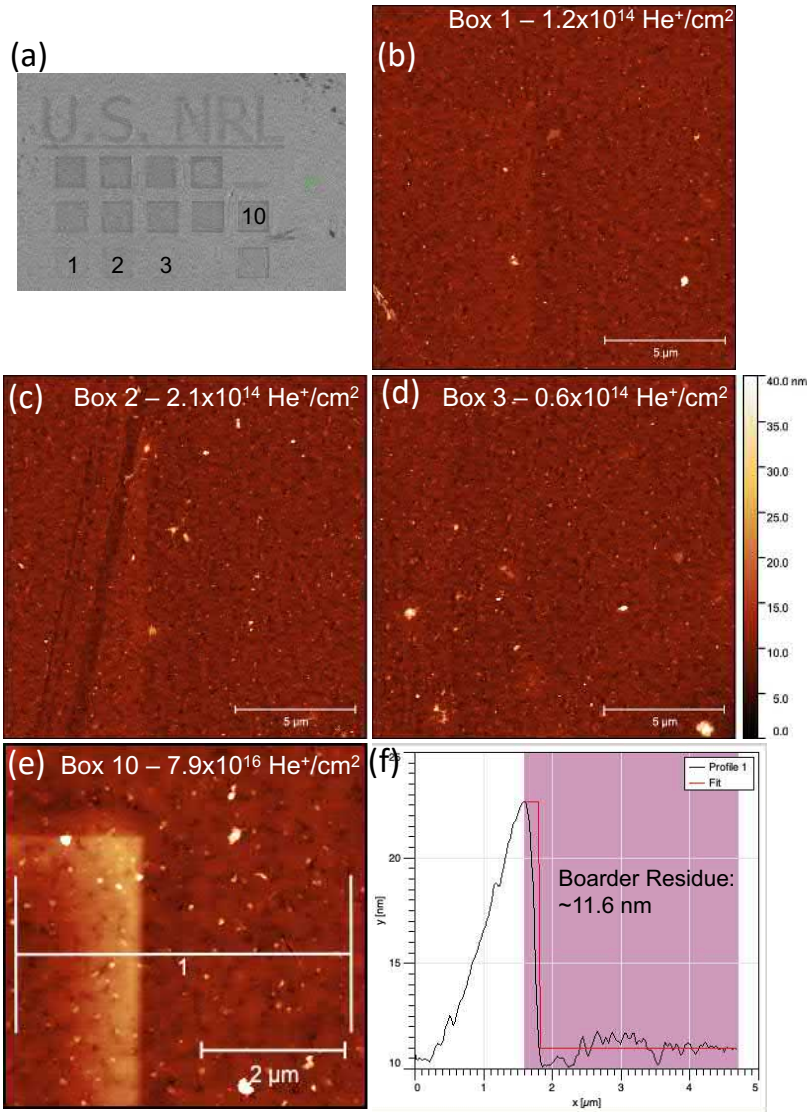

Figure S2. (a) Helium ion micrograph showing 20 µm × 20 µm square dose array patterning, with box numbers labeled. (b-e) (Box 1, 2, 3, and 10) AFM height maps taken in the upper right corner of the boxes coinciding with the labels shown in (a). (f) AFM height cross section coinciding with scan length label "1" in (e) showing carbon residue deposit peak height of 11.6 nm from the highest dosed square, but is confined to the edge of the feature.

In Figure S3 we overlay the Fe and Rh vacancies generated per He^+ per Å as a function of position within the film. These vacancy generation rates include the number of direct He^+ ion primary knock-ons, which is the number of atoms recoiling following a He^+ interaction, and the additional vacancies created by the Fe and Rh recoils. The maximum number of He^+ recoils occurs near 1000 Å, the center of the FeRh film and just prior to the projected He^+ range. The peak vacancy generation rate occurs before this depth (near 800 Å) because the energy of the Fe and Rh recoils is higher, enabling them to create a larger number of additional vacancies. The mean defect generation rate for Fe and Rh is approximately 0.052 Vac/Å·ion for each and the total number of vacancies generated per ion in a 2000 Å FeRh (50/50) film is 212 vacancies. The bar graph overlaid in the figure illustrates the normalized final He^+ distribution after coming to rest in the film. The peak concentration of He, now neutralized, occurs at approximately 1100-1250 Å into the film.

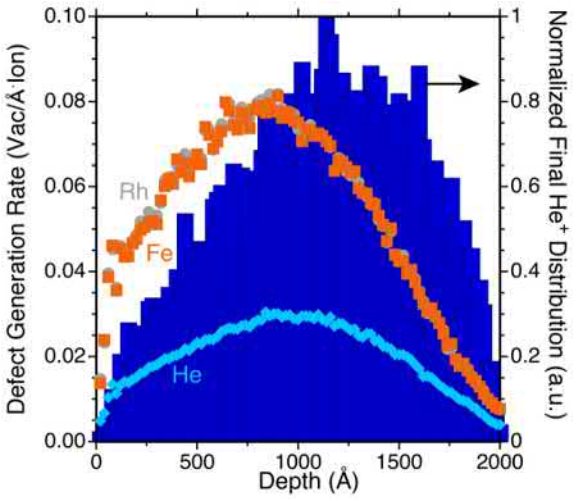

Figure S3. Data points (left y-axis): vacancy generation rate for Fe and Rh along with the number of He^+ induced primary knock-ons. Bar graph (right y-axis): normalized final He ion distribution in FeRh.

Figure S4 contains MOKE microscopy images at 300 K and at 235 K, 150 K, 100 K, and 7 K, as the sample is cooled. At room temperature, all of the patterns except for the lowest doses along the first row (including 1.0×10^{14}, 3.5×10^{14}, 6.0×10^{14}, and 8.5×10^{14} He^{+}/cm^{2}) are apparent in the MOKE image. As the temperature is cooled, additional patterned regions from the MOKE image disappear beginning at 235 K and the trend continues down to 7 K. These results confirm that the FeRh metamagnetic transition still occurs in the higher dosed samples, yet the transition occurs below room temperature. Therefore, even at these higher doses, sufficient magnetic order is preserved to induce the transition from ferromagnetic to antiferromagnetic at lower temperatures.

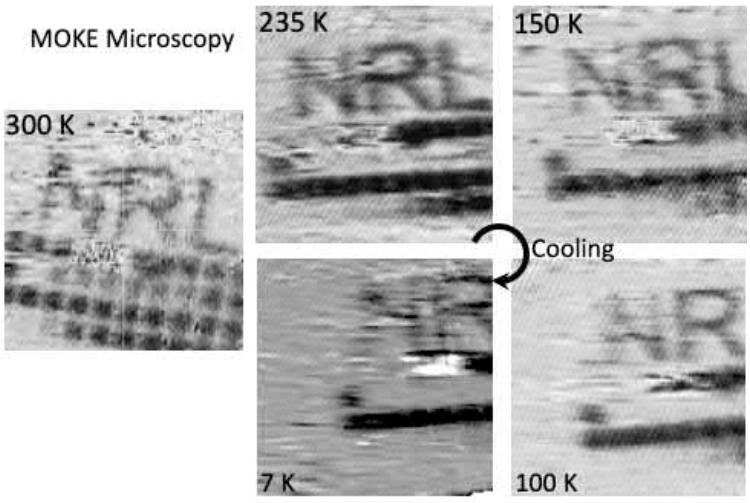

Figure S4. Temperature dependent MOKE imaging of a He^{+} dose array pattern with temperatures labeled. The pattern consists of 20 μm × 20 μm squares separated by 5 μm, with doses ranging from 1×10^{14} to 2.3×10^{15} He^{+}/cm^{2} along the first row and the second row ranging from 2.5×10^{15} to 4.7×10^{15} He^{+}/cm^{2}. Contamination of the helium ion microscope tip occurred during patterning of the third row causing wide fluctuations in beam current making the dose for those features unknown.

In Figure S5 we provide the abs(contrast) as a function of temperature from optical microscopy images during heating (red) and cooling (blue).

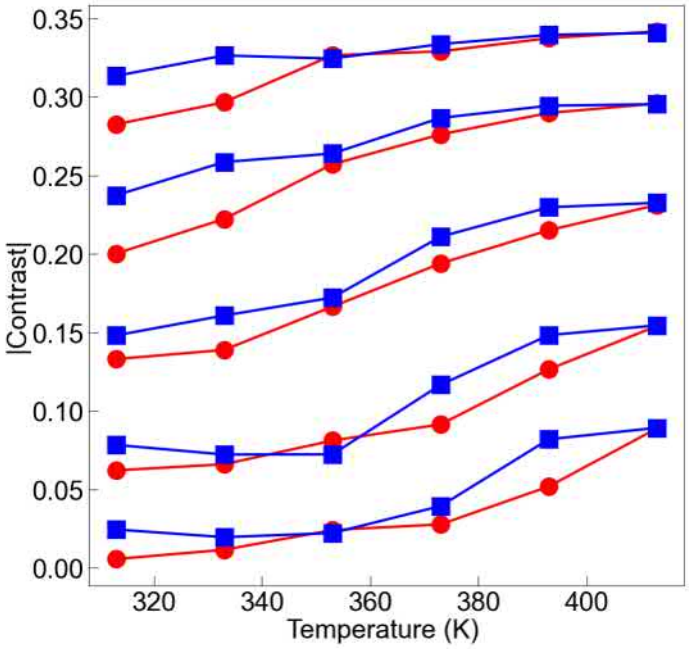

Figure S5. Optical contrast magnitude as a function of temperature for each image shown in Figure 4(a) of the main text. The red circles and blue squares correspond with images collected during heating and cooling, respectively. Starting from the bottom pair of lines the doses correspond to 1.1×10^{14} He^{+}/cm^{2}, 2.2×10^{14} He^{+}/cm^{2}, 4.0×10^{14} He^{+}/cm^{2}, 6.2×10^{14} He^{+}/cm^{2}, and 8.0×10^{14} He^{+}/cm^{2}. Each data set is offset by 0.05 units.

In Figure S6 we provide additional CAFM data of our nanoscale patterned structures. Figure S6(a) contains the height map corresponding with the current map from Figure 5(e) of the main text. It is apparent that there are approximately 1 nm depressions in the FeRh film corresponding with the location of each current peak. As noted in the text, the number of ions implanted into each spot corresponds with the total number of ions spread over the full area of the

25 nm features. Figure S6(b) contains a large area CAFM current map of the nanoscale feature arrays. At this scale, the 200 nm, 100 nm, and 50 nm patterned regions are all clearly distinguishable within each of the square arrays. In Figure S6(c,d) we provide the AFM height and current maps, respectively, for the 25 nm / 50 nm square array. There is some correlation between height and current, yet in contrast to the spot array, many regions appear to be increased above the background height rather than showing a depression. The lateral dimensions are indeed close to the designed dimension of 25 nm on a 50 nm pitch (i.e., 25 nm spacing). In the vertical direction, the features are elongated and in some instances appear to touch. We suspect the origin of this is two-fold. First, the focus of the beam may not have been perfectly circular, slight elongation (i.e. astigmatism) along the y-axis would skew the feature shape. This would also explain the elongation along this direction for the spot array features. The second source of elongation may originate from the raster procedure of the NanoFab HIM. Following each point, the beam is electrostatically blanked before moving to the next point and repeating. If beam blanking occurs along the raster direction then it could be the source of additional ions. The fact that this occurs for the spot array and the rastered patterns likely points to beam focus / astigmatism as the primary cause.

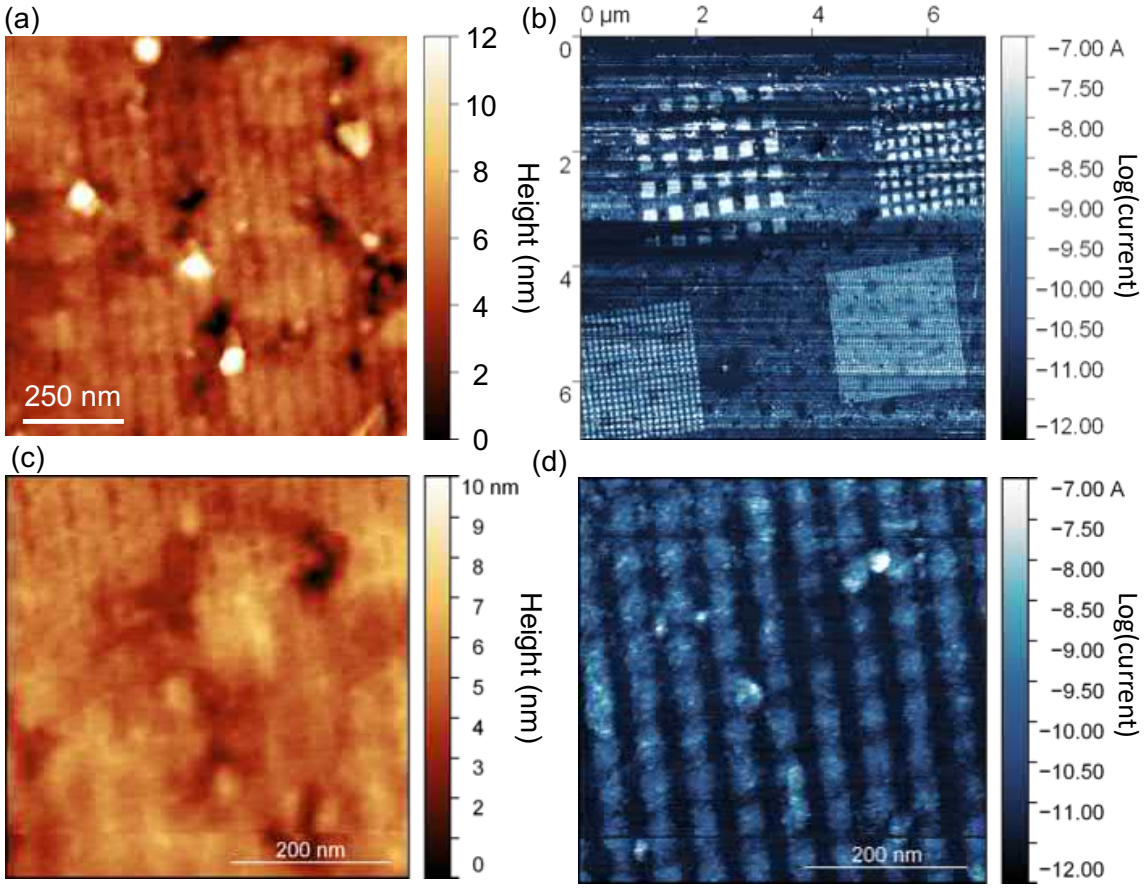

Figure S6. (a) AFM height map of the spot array sample corresponding with the current map from Figure 5(e) of the main text. (b) Log current map depicting regions of the four 2 µm × 2 µm nanoscale feature arrays consisting of squares / pitches of: upper left 200 nm/400 nm, upper right 100 nm / 200 nm, lower left 50 nm / 100 nm, and lower right 25 nm / 50 nm. (c) AFM height map and (d) current map of the array designed to have 25 nm squares spaced with a 50 nm pitch.